Journal of Materials Chemistry

Cite this: *J. Mater. Chem.*, 2011, **21**, 14240

www.rsc.org/materials

PAPER

Hierarchical structure and polymorphism of a sphere-cubic shape amphiphile based on a polyhedral oligomeric silsesquioxane–[60]fullerene conjugate†

Hao-Jan Sun,[a] Yingfeng Tu,*[b] Chien-Lung Wang,[a] Ryan M. Van Horn,[a] Chi-Chun Tsai,[a] Matthew J. Graham,[a] Bin Sun,[c] Bernard Lotz,[d] Wen-Bin Zhang*[a] and Stephen Z. D. Cheng*[a]

Received 4th March 2011, Accepted 1st April 2011
DOI: 10.1039/c1jm10954e

A shape amphiphile composed of covalently linked spherical and cubic nanoparticles with distinct symmetry ([60]fullerene (C_{60}) and polyhedral oligomeric silsesquioxane (POSS)) was synthesized and its solid state structures were characterized. The two types of nanoparticles are known to be generally immiscible, but they were connected with a short covalent linkage forming an organic–inorganic dyad (POSS–C_{60}) which exhibited interesting crystallization characteristics. Crystals of the dyad exhibited polymorphism with two different crystal structures: an orthorhombic and a hexagonal unit cell with symmetry groups of $P2_12_12$ and $P6$, respectively, both of which formed an alternating bi-layered structure of POSS and C_{60}. The different symmetry groups in the polymorphs were attributed to the different packing orientations of the POSS within each layer. In the orthorhombic unit cell, one set of the edges of the POSS moieties is parallel to the *c*-axis; while in the hexagonal unit cells the body-diagonal is parallel to the *c*-axis of the crystal. Based on the crystal packing structure and density differential, it has been determined that the hexagonal unit cell structure is the more thermodynamically stable phase. This type of bi-layered structure with an alternating conductive fullerene and insulating POSS layer structure is of great interest for various potential applications such as nano-capacitors.

Introduction

An aim of functional materials is the amplification of intrinsic atomic and molecular level functionalities to the macroscopic property level through rational design.[1–3] In most cases, atomic and molecular level functionalities seldom directly translate to the macroscopic material properties. Achieving direct correlation between molecular and macroscopic properties usually requires amplification through hierarchical structures across different length scales.[4] The formation of such hierarchical structures is a delicate balance of the free energy minimum (thermodynamics) and the transition pathway (kinetics) between the current and final state guided by physical principles such as specific interactions and entropic factors.[5,6] It thus becomes a critical step in the rational development of materials to understand and engineer distinct one-, two-, and three-dimensional hierarchical structures across different length scales to guide the transformation process and direct the amplification of targeted functions.

One of the intriguing targets in material science is the design, synthesis, and self-assembly of nano-hybrids, such as shape amphiphiles, based on various nano-building blocks with distinct 3D shape, chemical composition, and functionalities.[7–10] Shape amphiphiles usually refer to molecules possessing differences in the shape of the molecular moieties.[7] Understanding the role of distinct nano-building blocks in the crystallization of nano-hybrids with respect to their molecular functions, direction and magnitude of interactions, as well as their overall sizes and shapes will be essential for constructing supramolecular hierarchical structures at different length scales.[8] Two nano-particles of high symmetry and distinct chemical composition with potential for practical applications are polyhedral oligomeric silsesquioxanes (octaisobutyl–POSS, **1**)[11] and [60]fullerene (C_{60}, **2**) (Scheme 1).[12–16] POSS is an inorganic, cubic-shaped silica nanoparticle with a diagonal length of around 1.0 nm and a tunable overall molecular size depending on the size of the side groups.[11] It has been recognized as a potent material modifier for the next generation of

[a]*College of Polymer Science and Polymer Engineering, Department of Polymer Science, The University of Akron, Akron, OH, USA 44325. E-mail: wz8@zips.uakron.edu; scheng@uakron.edu*
[b]*College of Chemistry, Chemical Engineering and Materials Science, Soochow University, Suzhou, 215123, PR China. E-mail: tuyingfeng@suda.edu.cn*
[c]*State Key Lab for Chemical Fibers & Polymer Materials, Donghua University, Shanghai, 201620, PR China*
[d]*Institut Charles Sadron, 23, Rue du Loess, Strasbourg, 67034, France*

† Electronic supplementary information (ESI) available: Fig. S1–S7 and Tables S1 and S2 which include ^{1}H NMR spectrum, ^{13}C NMR spectrum, HSQC NMR spectrum, MALDI-TOF Mass spectrum, FT-IR spectrum, UV-vis absorption spectrum, TGA diagram, tilted ED pattern of hexagonal crystal form, and crystallographic parameters of Type I and II crystals. See DOI: 10.1039/c1jm10954e

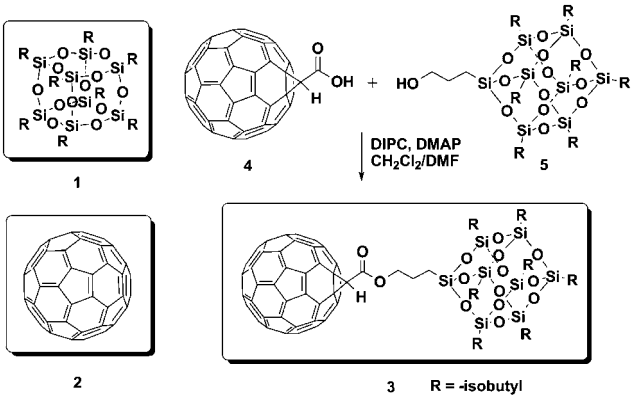

Scheme 1 Chemical structures of octaisobutyl–POSS (**1**), C_{60} (**2**) and POSS–C_{60} (**3**) and the synthetic route to POSS–C_{60} (**3**).

nano-composite plastics because of its good toughness, low dielectric constant, and excellent biocompatibility.[14,20] On the other hand, C_{60} is a carbon allotrope composed of 60 carbon atoms organized in a spherical shape with a diameter of ~1 nm.[12] It has received extensive attention due to its excellent electrical, magnetic, optical, and biological properties.[16] While the two particles share the common features of rigid conformation and incompressibility, their extremely different chemical compositions make them generally immiscible. Based on the potential hierarchical structures and electronic properties that might arise from the combination of C_{60} and POSS, a sphere-cubic shaped amphiphile was designed and synthesized to study its self-assembling behaviour and the resultant hierarchical structures. Recently, we have explored the synthesis and phase structures of a series of nano-hybrids based on POSS, C_{60}, polymers, and other electronic-active materials and showed that they are very versatile in self-assembly in the bulk and in solution, leading to a variety of structures and morphologies.[17–19] POSS–C_{60} dyads containing fulleropyrrolidines and iminofullerenes have been reported by Clarke *et al.*[21,22] In the work presented here, a short and simple covalent linkage was specifically chosen to connect the two nanoparticles to impart constraints on their packing (Scheme 1), so that the difference in molecular shapes, the immiscibility between POSS and C_{60}, and their interplay could lead to fine differences in molecular packing and structures.

In this article, we report on the design, synthesis, and crystallization of a sphere-cubic shaped amphiphile based on POSS–C_{60} (**3**). The dyad **3** was found to form crystals with two different crystal lattices: orthorhombic and hexagonal. The polymorphism is discussed in terms of their formation mechanism, crystal structure, and relative thermodynamic stability. In both crystal structures, an alternating bi-layered structure consisting of two layers of POSS and two layers of C_{60} exists with a layer thickness of ~2 nm. However, the packing of POSS and C_{60} within their individual layers is found to be very different, which seems to be dependent upon the building block's symmetry. These structures are hierarchical in nature and promising for a variety of applications. In particular, the alternating arrangement of semiconducting C_{60} layers and insulating POSS layers is ideal as nano-capacitors with nanometre spacing constructed directly by self-assembly.

Experimental section

Chemicals and solvents

3-Hydroxypropylheptaisobutyl–POSS (**5**), 4-(dimethylamino)-pyridine (DMAP, 99%), *N*,*N*′-diisopropylcarbodiimide (DIPC, 99%), dichloromethane (CH_2Cl_2, anhydrous, ≥99.8%), and *N*, *N*-dimethylformamide (DMF, anhydrous, 99.8%) were purchased from Aldrich and used as received without further purification. [60]Fullerene (C_{60}, 99.9%) was purchased from MTR Ltd. and used as received. The carboxylic acid derivative of methanofullerene (**4**) was synthesized through the hydrolysis of *tert*-butyl [60]fullerenoacetate according to the literature.[23,24]

Synthesis of POSS–C_{60} dyad 3

To a solution of **4** (380 mg, 0.50 mmol) in 16 mL of CH_2Cl_2/DMF mixed solvent (v/v = 15/1), **5** (430 mg, 0.50 mmol) and 4-(dimethylamino)pyridine (DMAP, 61 mg, 0.50 mmol) in 8 mL toluene were added followed by *N*,*N*′-diisopropylcarbodiimide (DIPC, 130 mg, 1.03 mmol). The mixture was stirred at room temperature for 24 h. After that, the solution was washed with H_2O (10 mL) and brine (10 mL). The organic phase was dried over $MgSO_4$ and then concentrated to give crude product. After column chromatography with silica gel using hexane/toluene (v/v = 2/1) as eluent, **3** was obtained as a dark brown powder (572 mg). Yield: 70%. ^{1}H NMR (300 MHz, $CDCl_3$, Fig. S1†): δ (ppm) 4.80 (s, 1H), 4.45 (t, 2H), 1.98 (m, 2H), 1.89 (m, 7H), 0.98 (m, 42H), 0.83 (m, 2H), 0.64 (m, 14H). ^{13}C NMR (75 MHz, $CDCl_3$, Fig. S2†): δ (ppm) 148.6, 146.1, 145.8, 145.5, 145.5, 145.4, 145.4, 145.3, 145.0, 145.0, 145.0, 144.9, 144.8, 144.7, 144.2, 144.0, 143.5, 143.3, 143.3, 143.3, 143.2, 143.2, 143.1, 142.7, 142.5, 142.4, 142.3, 141.4, 141.2, 140.8, 136.6, 70.9, 68.7, 39.5, 22.5, 8.8. FT-IR (KBr) ν (cm^{-1}): 1741 (C=O), 1261 (Si–C), 1229 (C–O), 1099 (Si–O), 524 (C–C in C_{60}). MS (MALDI-TOF): calcd monoisotopic mass for $C_{93}H_{70}NaO_{14}Si_8$ = 1657.3 Da; found: *m*/*z* 1657.8 (100%) (MNa^+).

Sample preparation and characterizations

All NMR experiments were performed in $CDCl_3$ (Aldrich, 99.8% D) on a Varian Mercury 300 NMR spectrometer. The ^{1}H NMR spectra were referenced to the residual proton impurities in $CDCl_3$ at δ 7.27 ppm. The ^{13}C NMR spectra were referenced to $^{13}CDCl_3$ at δ 77.00 ppm. Infrared spectra were recorded on an Excalibur Series FT-IR spectrometer (DIGILAB, Randolph, MA) by casting polymer films on KBr plates from polymer solutions with subsequent drying. The data were processed using Win-IR software. Matrix-assisted laser desorption/ionization time-of-flight (MALDI-TOF) mass spectra were recorded on a Bruker Ultraflex III TOF/TOF mass spectrometer (Bruker Daltonics, Billerica, MA), equipped with a Nd:YAG laser emitting at a wavelength of 355 nm with *trans*-2-[3-(4-*tert*-butylphenyl)-2-methyl-2-propenylidene]malononitrile (DCTB, Aldrich, >99%) as the matrix in $CHCl_3$ at a concentration of 20 mg mL^{-1}.

The single crystals of **3** were obtained by slow evaporation from dilute solution on various substrates in a solvent-saturated atmosphere. A chamber with a THF saturated atmosphere was constructed in a vial with a steel cylindrical mount at the bottom

and 1 mL of THF at the bottom of the vial. A square substrate of about 1.0 × 1.0 cm^2 (various materials) was placed on the top of the mount and the vial was sealed with a rubber stopper. The sealed chamber was kept at room temperature for 1 hour for the atmosphere to reach THF saturation. The solvent was allowed to evaporate through the interface between the rubber cap and the vial wall. The evaporation rate was controlled by the tightness of the rubber cap. A micro-syringe was used to deposit one drop of the dilute solution on the substrate through the rubber cap. The chamber was then left to allow for the solvent to completely evaporate. The single crystals on the substrate were examined by phase contrast microscopy (PCM, Olympus BX52) and then collected for characterization using a variety of techniques.

A small amount of crystals (~0.5 mg) was collected for density measurement. The sample was placed in a vial with water followed by ultrasonication to remove the air bubbles embedded within the sample. After that, the sample sank to the bottom of the vial due to high density. Potassium iodide (KI) was then added into the solution stepwise with ~0.1 g at a time to gradually increase the solution density at the interval of at least 20 min to ensure the equilibrium within the solution. When the sample started to suspend in the middle of the solution, the density of the sample is identical to that of the solution which can be easily determined.

Differential scanning calorimetry (DSC, Perkin-Elmer PYRIS Diamond with Intracooler 2P cooling system) experiments were carried out to observe possible phase transitions. The samples were grown as stated above and collected in a DSC pan with a weight of typically 3 mg. The samples were then heated at a rate of 10 °C min^{-1} from 25 °C to 320 °C (80 °C below the onset temperature for weight-loss as determined by Thermogravimetric Analysis).

One-dimensional (1D) wide angle X-ray diffraction (WAXD) experiments were conducted using a Rigaku Multiflex 2 kW automated diffractometer using Cu Kα radiation (0.1542 nm) in reflection mode. The detector scanning rate was 1° per minute, and the 2θ angle was ranged between 1.7° and 20.0°. The peak positions were calibrated using silicon powder in the high angle region (>15°) and silver behenate in the low angle region (<15°). Background scattering was subtracted from the sample patterns. In order to observe different types of crystal, various solution evaporation rates were applied (from slow to very slow) to form single crystal mats either directly on the X-ray sample holder or in a well sealed vial before being deposited onto the X-ray sample holder.

For transmission electron microscopy (TEM, Philips Tecnai 12 at an accelerating voltage of 120 kV) experiments, the single crystals were prepared on a carbon coated glass surface. One drop of poly(acrylic acid) 25% aqueous solution was placed on the surface and let to dry to grab the carbon film underneath. The dried, hardened droplet along with the film was removed by a razor blade. Then the droplet was transferred onto a water surface with PAA side touching the water. After a few minutes, the PAA dissolved and the carbon film was in contact with the water surface. Clean TEM copper grids (400 mesh, SPI) were then used to pick up the film. Before TEM observation, samples were put into a vacuum oven for 12 hours to remove the residual solvent and moisture. Bright field (BF) images and selective area electron diffraction (SAED) patterns were then taken. The *d*-spacings were calibrated using a TlCl standard.

Molecular modelling and diffraction pattern analyses of crystal structures were conducted on the Accelrys Cerius^2 software package. The lowest energy conformation of a POSS–C_{60} dyad in vacuum was chosen as the starting conformation. Basic unit cell parameters determined by crystallographic experimental data from 1D WAXD and SAED experiments were used to build the unit cell. The positions of atoms in this unit cell were judged by comparing the calculated ED patterns with the experimentally observed patterns.

Results and discussions

Molecular design and synthesis of POSS–C_{60} (3)

The molecule was designed to expand the understanding of POSS and C_{60} nanoparticles in terms of their symmetry and interactions. Structurally, C_{60} possesses I_h symmetry in three dimensions and the POSS without a side group has an O_h symmetry.[25,26] Both individual particles are highly crystalline in the solid state. Depending on the periphery substituents, POSS exhibits different crystal structures. The octaisobutyl-POSS (**1**) crystal structure is triclinic.[27,28] The periphery substituents also play an important role in determining the POSS–POSS interactions.[19] For isobutyl side groups, only weak van der Waals forces exist. In contrast, C_{60} exhibits a strong tendency for irregular self-aggregation due to its isotropic shape and strong π–π interaction. Known as a plastic crystal above −17 °C, C_{60} forms a face-centered-cubic structure at room temperature.[29,30] Owing to their distinct natures, the two particles exhibit strong segregation when blended. By forcing the two nanoparticles together with a short, simple covalent linkage, macroscopic phase separation can be inhibited. The symmetry of the constituent particles is thus broken and only the rotational symmetry along the molecular long axis is preserved. In dyad **3**, the POSS moiety only possesses C_{3v} symmetry with the C_3 axis going through the diagonal silicon atoms of the POSS cage, while the C_{60} moiety only possesses C_v symmetry. The versatility of periphery functionalization on the POSS cage allows further fine tuning of the size of the POSS particle and the interaction between POSS particles. Hence, it is interesting to study how these dyads with covalent confinement and broken symmetry assemble into crystals. In this article, we will mainly focus on the simplest dyad **3** with nonfunctional isobutyl substituents.

The dyad **3** was synthesized from two readily available starting materials by Steglich esterification.[31] The carboxylic acid functionalized C_{60} (**4**) was synthesized from C_{60} according to procedures in the literature and the hydroxyl-functionalized POSS (**5**) is commercially available.[23,24] The esterification was performed in a mixed solvent of CH_2Cl_2/DMF due to the low solubility of **4** in either of the single solvents. The reaction proceeded with high efficiency and the product was readily purified by chromatography with a 70% yield. The dyad **3** was obtained as a dark brown powder stable toward singlet oxygen and can be handled without special precaution to exclude oxygen. It is highly soluble in common organic solvents, such as hexane, THF, chloroform, and toluene (>300 mg mL^{-1}). The unusually high solubility of this C_{60} derivative can probably be attributed to the isobutyl groups on the POSS cage.

The dyad **3** was fully characterized by ^{1}H NMR, ^{13}C NMR, FT-IR, and MALDI-TOF mass spectroscopy (also see ESI†). In the ^{1}H NMR spectrum, the appearance of a triplet at δ 4.45 ppm is characteristic of the methylene protons adjacent to the ester bond. In the ^{13}C NMR spectrum, the sp^2 carbons on C_{60} can be clearly seen at δ 136.6–148.6 ppm and the sp^3 carbons of isobutyl groups on the POSS cage are evident at δ 25.9, 24.1, and 22.7 ppm. The formation of the ester bond is also supported by the strong carbonyl absorption in the FT-IR spectrum at 1741 cm^{-1}. Moreover, the MALDI-TOF mass spectrum revealed a *m/z* of 1657.8, which matches well with the calculated 1657.3 Da for $C_{93}H_{70}Si_8O_{14}Na$. All of these results confirm the success of esterification and the formation of the proposed chemical structure. Further characterization of **3** by HSQC NMR experiments, UV-vis absorption spectrometry, and thermal gravimetric analysis reveals the detailed assignment of the chemical structure, the essentially unchanged optical properties of C_{60}, and the high thermal stability of the dyad. The data can be found in the ESI†.

Crystal polymorphism of 3 in solid state

The solid state phase transitions of **3** were first determined by DSC. Fig. 1a shows a DSC heating diagram for a crystalline sample of **3** obtained by slow evaporation of its dilute solution in THF at an initial concentration of 0.2% (w/v) under a solvent-saturated atmosphere on a variety of substrates including aluminium, bare or carbon-coated mica, bare or carbon-coated glass, and silicon wafer. Two endothermic peaks can be clearly seen at 244 °C and 269 °C, respectively, which can be due to either the existence of two different crystal forms with different melting temperatures (polymorphism) or of one crystal form with two distinct metastabilities (such as two different crystallite sizes). The latter possibility is less likely, since it is very difficult and rare to have two distinct populations of specific crystallite sizes *via* normal solvent evaporation and crystallization processes. Since DSC does not provide any structural information, a definite proof of the first assumption would require the investigation of the growth conditions to identify each crystal form and then, determine the crystal structures using various structure-sensitive experiments, such as WAXD and SAED.

Fig. 1b and c show two distinct crystal morphologies observed under PCM. The first type of crystal (Type I) exhibits an elongated lathe-like habit (Fig. 1b) and was found to grow predominantly and most easily on a silicon wafer by slow evaporation of dilute solutions of **3** in THF. The crystal habit is apparently highly anisotropic and the epitaxial growth of the "daughter" crystals was found at 90° from the "mother" crystals. The second type of single crystal (Type II) exhibits a hexagonal shape as shown in Fig. 1c, and was found to grow easier on the amorphous carbon surface at much slower evaporation rates than Type I crystals. It should be noted that even under this condition, Type I crystals could still form, though at relatively low concentrations.

The highly anisotropic Type I crystal habit is a result of the different crystal growth rates along the normal direction of the crystalline planes. From the length-to-width ratio, the growth rate along the long axis of the crystal is estimated to be more than 10 times faster than that along the width direction. Since the symmetry of single crystal morphology usually reflects that of the single crystal unit cell, this observation suggests that the crystal unit cell must possess a 2_1 rotational symmetry.[6,32,33] The hexagonal shape of Type II single crystals, on the other hand, reveals that the crystalline plane at the growth fronts possesses identical growth rates, and they must be belong to the same set of (*hkl*) crystalline planes. The rotational symmetry of this single crystal unit cell is most likely 3_1 or 6_1.[6,33] The co-existence of two distinct crystal morphologies clearly indicates the polymorphism of **3**.

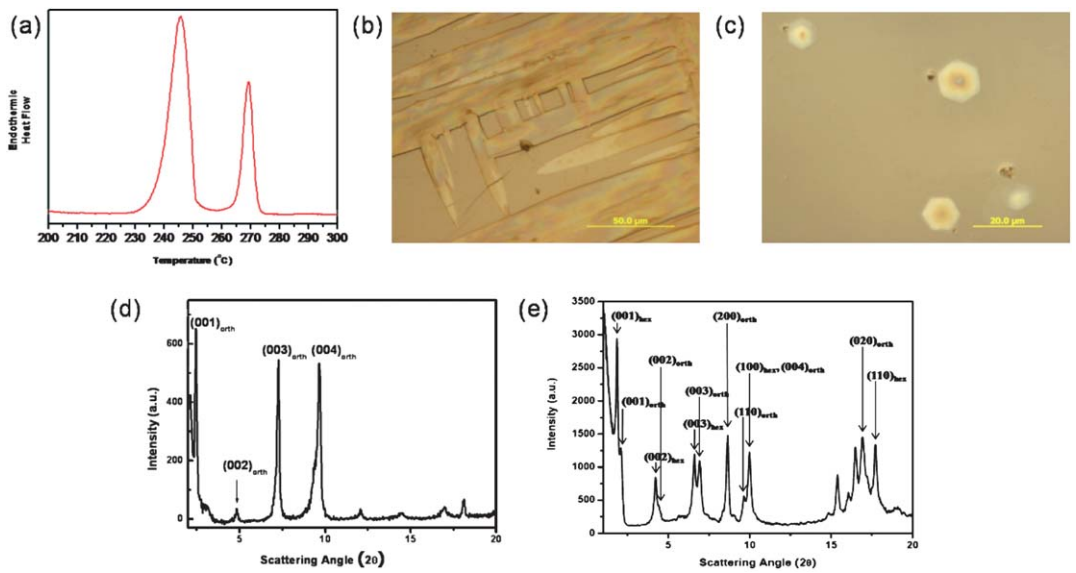

Fig. 1 (a) DSC scan of crystalline samples of dyad **3**; (b) Type I crystal: elongated lathe-like crystals observed under PCM (scale bar: 50 μm); (c) Type II crystal: hexagonal crystals of **3** observed under PCM (scale bar: 20 μm); (d) 1D WAXD pattern of Type I crystals with a flat-on arrangement on the substrate; and (e) 1D WAXD powder pattern of a mixture of Type I and II crystals (*orth* represents orthorhombic lattice and *hex* denotes hexagonal lattice).

Evidence of the polymorphism is further provided by 1D WAXD results of these two types of crystals (Fig. 1d and e). Fig. 1d is the 1D WAXD pattern obtained in reflection mode of the crystals directly grown on the aluminium sample holder by a slow solvent evaporation process that mostly grows Type I crystals. Since the samples are single crystal-like with a flat-on arrangement, such an experimental setup mainly provides information on their periodic structures along the vertical (substrate normal) direction. Strong diffraction peaks are observed, and their q ratios of 1 : 2 : 3 : 4 suggest a layered structure perpendicular to the substrate normal. These diffractions can be used to determine the c-axis dimension of the unit cell. The first sharp diffraction peak at the smallest diffraction angle ($2\theta = 2.44°$) corresponding to a d-spacing of 3.62 nm is tentatively assigned as the (00l) diffraction. Higher ordered diffractions are also observed at d-spacings of 1.81 nm as the (002), 1.21 nm as the (003) and 0.905 nm as the (004) diffraction, respectively. The relatively low intensity of the (002) diffraction is due to the fact that the bi-layered structure is symmetric along the c-axis. If it was perfectly symmetric, the (002) diffraction would be extinct.

Fig. 1e, on the other hand, shows a more complicated 1D WAXD pattern obtained from a mixture of Types I and II crystals in reflection mode. In this case, the samples were prepared on an amorphous carbon surface at a much slower evaporation rate than the previous one. The majority of the crystals are thus Type II. After complete evaporation, the crystals were transferred to the WAXD sample holder. Hence, this is a powder pattern with random crystal orientation. Compared with Fig. 1d, there appears to be a new set of diffractions in addition to the first set of the diffraction peaks discussed above. The d-spacing of the first diffraction in this set of new diffraction peaks is found to be 4.27 nm. The second and third diffraction peaks also fit to the q ratios of 1 : 2 : 3, indicating that the first diffraction belongs to the (001) and the corresponding higher orders are the (002) and (003) as being identified in Fig. 1e. Based on their q ratios, this set of newly observed diffraction peaks can also be attributed to another layer structure with different layer spacings from the previous one. Notably, the d-spacings of these two (001) diffractions (3.62 nm and 4.27 nm) are both longer than the length of the long center axis of the dyad **3** (1.62 nm). The existence of two sets of layer structures again confirms the crystal polymorphism of **3**. Further work is needed to determine the crystal structure and symmetry group for each of the crystals, and reveal their formation mechanism and relative thermodynamic stability.

Type I crystal form: an orthorhombic lattice

Fig. 2a is a BF TEM image (without staining) of a tip of a Type I single crystal. Fig. 2b is a SAED pattern with the [00l] zone obtained from this single crystal. The extinct spots of the odd h-values at the (h00) and the odd k-values at the (0k0) indicate that this 2D lattice possesses the ($p2gg$) (No. 8) symmetry.[25] The two dimensions of the unit cell can thus be determined as $a = 2.10$ nm and $b = 1.05$ nm. Although the dimension of the b-axis is half that of the a-axis, the unit cell is not square but rather rectangular based on the symmetry rule. These unit cell dimensions also explain the observation of 90°-epitaxial growth in Type I crystals (Fig. 1b).

In order to determine the c-axis dimension, a tilted ED pattern is necessary. Fig. 2c shows an ED pattern obtained when the crystal is tilted by 30° along the b*-axis at which the (202) diffraction spot appears. The d-spacing of the (202) plane is measured to be 0.91 nm. Therefore, the c-axis dimension can be calculated to be 3.62 nm, which fits very well with that of the assigned (001) diffraction peak in Fig. 1d and confirms again the parallel arrangement of the layered structure relative to the substrate surface. Density measurements show that the crystals have a density of 1.34 g cm^{-3}, indicating four molecules per unit cell ($Z = 4$, $\rho = 1.36$ g cm^{-3}). Combined with the limiting conditions for the (h00) and the (0k0) extinction, the space groups are determined to be $P2_12_12$ (No. 18).[25] Therefore, this is an orthorhombic unit cell with the dimensions of $a = 2.10$ nm, $b = 1.05$ nm and $c = 3.62$ nm. The diffractions in Fig. 1d and 2b can then be assigned accordingly.

Simulation utilizing the Accelrys Cerius^2 package with the universal force field method verified the determination of the structure and unit cell dimension. Fig. 3a–c show three projections of this orthorhombic unit cell with the space group of $P2_12_12$ along the [001], [100] and [010] directions, respectively. In this set of figures, totally sixteen molecules are included with a crystal dimension of a, 2b and 2c. The formation of the bi-layered structure in the crystal is evident, and the layer normal is parallel to the c-axis. Since this bi-layered structure adopts the head-to-head and tail-to-tail arrangements of the molecules (C_{60}s and POSSs are interacted to their own in the layer packing), each bi-layered structure thus contains double-layers of C_{60} and double-layers of POSS moieties.

Fig. 3a shows the zigzag-like arrangement of the C_{60} projections in the ab-plane (viewed along the c-axis) for the neighbouring molecules along the b-axis. This is similar to the structure of pristine C_{60} crystals (a fcc structure).[29,30] Since the C_{60}s are arranged to form the double-layer by themselves within the bi-layered structure, the projection of the ab-plane in this figure possesses four C_{60}s along the b-axis (see the numbers in Fig. 3a). Yet they are not located in the same ab-plane: two of them (numbers 1 and 3 in Fig. 3a) are located at the top layer of the C_{60}-double-layer with their POSS cages connected to the top POSS layer (colored in red-orange), and the other two (numbers 2 and 4 in Fig. 3a) are located at the bottom layer of the C_{60}-double-layer with their POSS cages connected to the bottom POSS layer (more clearly, see Fig. 3c). The neighbouring C_{60}s along the b-axis have thus a glide plane to slide b/2 along the b-direction, which leads to the packing of POSS cages into a simple square lattice in the ab-plane with a distance of 1.10 nm between two neighbouring POSS cages. If viewed the ac-plane along the b-axis (the [010] zone) direction, the projections of the POSS cages in their double-layer managed to have a packing scheme that the POSS in the top layer is normally set on the POSS in the bottom layer (Fig. 3c). However, when viewed the bc-plane along the a-axis as shown in Fig. 3b, the projections of the POSS cages in the top layer of their double-layer sit in-between the two neighbouring POSS cages in the bottom layer. This simulation data indicates again that within the double-layer of POSS cages, a glide plane exists, and it moves the POSS cages by the b/2 distance along the b-axis direction. Therefore, in a single bi-layer structure of the POSS cages, each POSS cage has four nearest POSS neighbours in the same layer with a center-to-center distance of 1.10 nm and another two in the adjacent layer with an even closer center-to-center distance of 1.05 nm. On the other hand, the center-to-center distance between two neighbouring C_{60}s in contact is 1.05 nm. This is slightly larger than that in pristine C_{60} (1.0 nm).[29] Therefore, the interaction between C_{60}s might not be optimized in this molecular packing. The

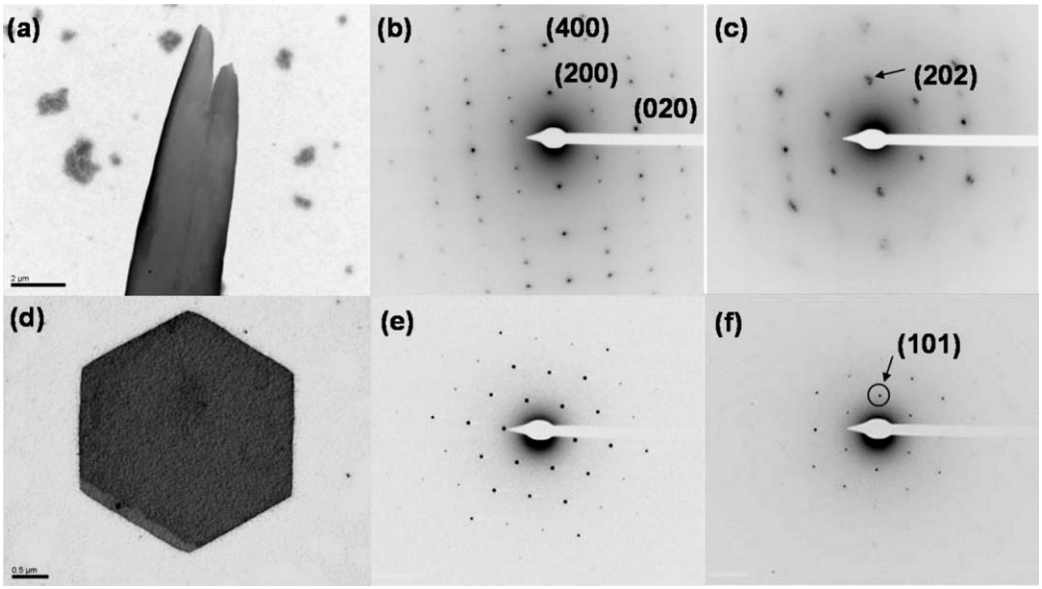

Fig. 2 TEM BF images of Type I (a) and II (d) single crystals of **3**; the orthorhombic ED pattern of the [00l] zone for Type I single crystal at 0° (b) and 30° (c) tilting angles; and the hexagonal ED pattern of the [001] zone for Type II single crystal at 0° (e) and 12° (f) tilting angles along the *b*-axis.

computer-simulated ED pattern from the [001] zone can be found in Fig. 3d. This pattern quantitatively agrees with the experimental ED pattern (Fig. 2b) and the intensities of diffraction spots also qualitatively match with the experimental observation. Therefore, Fig. 3a–c capture the overall symmetry group and molecular packing of dyad **3** in orthorhombic form.

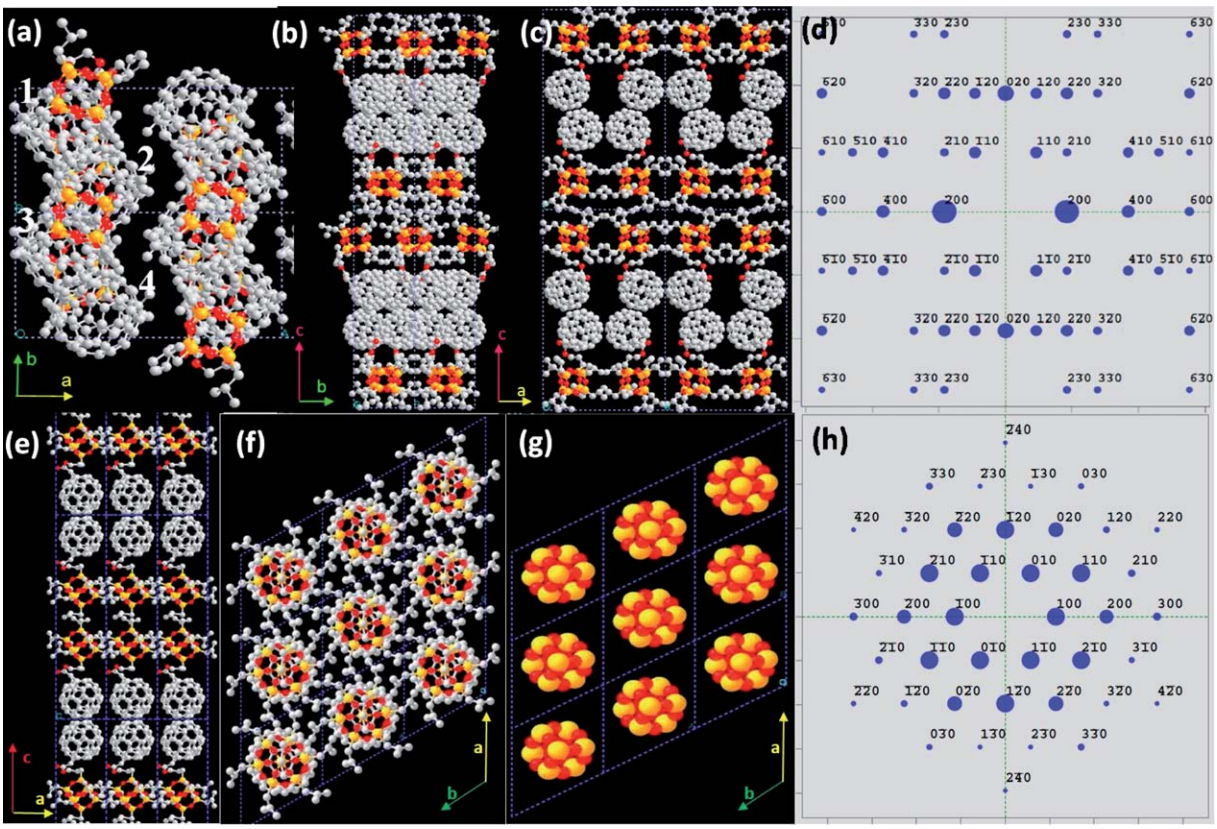

Fig. 3 Simulations of molecular packing in the orthorhombic crystal lattice of **3** on *ab*-plane when projected from *c*-axis direction (a), *bc*-plane when projected from *a*-axis direction (b), and *ac*-plane when projected from *b*-axis direction (c); and the computer-simulated ED pattern of the [001] zone (d). Projections of molecular simulated packing in the hexagonal crystal lattice of **3** on the *ac*-plane (e), the *ab*-plane (f). The packing of POSS cages in the crystal lattice is shown in (g) and the computer simulated ED pattern of the [001] zone in (h). The silver spheres represent C_{60} while the orange-red cubes represent POSS.

Type II crystal form: a hexagonal lattice

Type II crystals can only be formed with very slow evaporation rates and they are easier to form on hydrophobic substrates (*e.g.* carbon coated surfaces) than hydrophilic surfaces (*e.g.* glass or silicon wafer). The ED pattern in Fig. 2d is the [001] zone diffraction of Type II crystals with the electron beam parallel to the *c*-axis. The six-folded symmetry exhibits a hexagonal lattice in the *ab*-plane. The (100) *d*-spacing is measured to be 0.88 nm and the length of the *a*- and *b*-axis can thus be calculated to be 1.02 nm, indicating a close packing in the crystal lattice. The length of the *c*-axis is determined by utilizing tilted SAED experiments in TEM. With increasing tilting angle along the *b*-axis (Fig. S7b†), the (100) diffraction spot almost disappeared at 8° and the (101) diffraction spot appeared at 12° (Fig. 2f). The *d*-spacing of the (101) plane was measured to be 0.86 nm, corresponding to a *c*-axis dimension of 4.27 nm that fits well with the WAXD result deduced in Fig. 1e.

In the hexagonal crystal, the dimension of this *c*-axis reveals that the molecules also pack with a head-to-head and tail-to-tail arrangement. The **3** dyad now conforms to a cylindrical shape with the long axis perpendicular to the *ab*-plane, forming an alternating bi-layered structure perpendicular to the long axis. The packing in this case is closer than that in the orthorhombic unit cell, and this hexagonal crystal is about 0.90% higher in theoretical packing fraction compared with the orthorhombic crystal. Taking all of the structural information into consideration, the most probable space group is *P*6 (No. 168).[25] In the crystal, one motif contains two head-to-head molecules and the long axis of the motif is parallel to the lattice *c*-axis. Motifs locate at the six-fold axis in the *P*6 unit cell with a multiplicity of 1 and a site symmetry of 6 (the position "a" according to the Wyckoff letter).[25] Each unit cell contains one motif or two molecules. The experimentally measured density of 1.39 g cm^{-3} is in good agreement with the calculated density of 1.41 g cm^{-3}. Based on this unit cell dimension, the diffractions in Fig. 1e and 2e and f, such as the (100) and (110) diffractions, can also be assigned accordingly.

The packing of **3** in the crystal structure is also supported by simulation based on the universal force field method with the Accelrys Cerius^2 package. The result is shown in Fig. 3e–h. When viewed along the *b*-axis (the [010]) direction as shown in Fig. 3e, the bi-layered structure can be clearly seen with multiple columns of **3** in a hexagonal crystal unit cell. Within each layer, both POSS cages and C_{60}s are packed in the hexagonal lattice in the *ab*-plane. When viewed along the *c*-axis (the [001]) direction, each of them possesses six closest neighbours as shown in Fig. 3f. Notably, the body diagonal of the POSS cage is parallel to the *c*-axis and thus, the rest of the Si atoms form three fold symmetry when viewed along the *c*-axis of the crystal as shown in Fig. 3g. The center-to-center distance between C_{60}s is 1.02 nm, which is still slightly larger than that in pristine C_{60} crystals (1.00 nm) but closer than that in the orthorhombic unit cell (1.05 nm). It is probably due to the bulky isobutyl groups on the POSS cages that require more space to accommodate and thus slightly expands the unit cell dimension of C_{60} packing. The results also suggest that the C_{60}–C_{60} interactions in this case are stronger than in the orthorhombic unit cell. In addition, the computer-simulated ED pattern from the [001] zone (Fig. 3h) matches well with the experimental ED pattern (Fig. 2e). Therefore, this simulation in Fig. 3e and h is an accurate description of the overall symmetry and molecular packing of **3** in Type II crystals.

Comparison between the two distinct crystal forms

Now that the Type I and Type II crystal forms have been determined to be orthorhombic and hexagonal, respectively, we would like to compare them in terms of thermodynamic stability and structural formation kinetics. The calculated *d*-spacing and the experimentally observed *d*-spacing for both crystal forms are summarized and listed in Tables S1 and S2†, respectively. The density comparison (1.34 g cm^{-3} *vs.* 1.39 g cm^{-3}) and the higher melting point of hexagonal crystal form determined by DSC suggest that the hexagonal lattice should be thermodynamically more stable. Nevertheless, the metastable orthorhombic lattice is kinetically more favourable and easier to form. In other words, although the hexagonal crystal form possesses the global free energy minimum, its formation barrier is high; meanwhile, the orthorhombic crystal form only has a local free energy minimum, but the formation barrier is low, leading to a faster kinetic pathway.[5,6]

The hierarchical structure in these two crystal forms is also interesting. Although the two crystal forms are distinctly different, both form bi-layered structures with ~4 nm layer spacing along the long axis of the molecule in a head-to-head and tail-to-tail configuration. This packing scheme is not uncommon in the crystal or supramolecular structures of fullerene derivatives.[34–38] In this case, it is apparently due to the immiscibility between POSS and C_{60} and the constraints imposed by the covalent linkage. However, the detailed packing of these nanoparticles within each layer is very different for these two crystal forms. We speculate that the C_{60}–C_{60} interaction and the immiscibility between C_{60} and POSS are the major driving force for the crystallization and the POSS cage orientation within each layer may determine the crystal lattice and symmetry owing to its slightly larger molecular size. Specifically, when the orthorhombic crystals are formed, the edges of POSS are oriented either parallel or perpendicular to the *c*-axis, giving a C_2 or C_4 rotational symmetry. In this case, the C_2 symmetry dominates the molecular packing and crystal growth to construct the orthorhombic lattice. Nevertheless, the twice-longer *a*-axis with respect to the length of the *b*-axis still reflects the residual closeness of the C_4 symmetry. The rationale for this structural formation could be attributed to the POSS geometry when they form the first close-packed layer of the crystal on a silicon wafer. On the other hand, if the diagonal direction of POSS moieties is oriented along the *c*-axis, both C_{60} and POSS cage possess the C_{3v} symmetry, which can lead to a hexagonal packing scheme. As reflected by density measurements, the hexagonal lattice offers a higher density packing. It seems that the C_{60}–C_{60} interactions may dominate the crystal structural formation, since the hexagonal crystal growth is favoured on hydrophobic substrates such as a carbon-coated surface and requires much longer time for C_{60}s to maximize their interactions. The close packing of the C_{60}s in this case resembles a 2D hexagonal lattice. The diagonal orientation of the POSS cages serves to enhance the cylindrical symmetry and assists the formation of the hexagonal lattice. Therefore, it is evident that even though the format of these two

bi-layered structures on the nanometre scale is identical, their dimensions and the fine structures within each layer are very different, which leads to the difference in their thermodynamic stability.

Since C_{60} layers are semi-conductive or conductive upon doping and POSS layers are insulating, the electronic properties of such an alternating (semi-) conductive/insulating structure with a nanometre scale *d*-spacing (the *c*-axis: 3.62 nm in an orthorhombic form, and 4.27 nm in a hexagonal form) are of great interest. Together with the ability to grow macroscopic crystalline films, the "as-assembled" crystals are promising as nano-layered capacitors built up by the "bottom-up" approach. The relevant experiments including device fabrication and capacitance measurement are now ongoing in our laboratory and will be discussed in future publications.

Conclusions

In summary, we have reported the design, synthesis, and polymorphism of a sphere-cubic shaped amphiphile composed of an inorganic–organic, POSS–C_{60} dyad. These particles are generally immiscible. A short covalent linkage was thus chosen to connect the two building blocks and prevent macroscopic phase separation. Under different growth conditions, dyad **3** can crystallize into orthorhombic or hexagonal crystal lattices. The hexagonal phase was found to be thermodynamically more stable, while the orthorhombic phase is kinetically more favoured. The common feature in both crystal forms is the bi-layered structure along the *c*-axis of the crystals with nanometre *d*-spacings caused by alternating C_{60} and POSS layers. Depending on the growth conditions and environment, the packing of the two nanoparticles within each individual layer is of very different symmetry. With the POSS being an insulator and C_{60} being a semi-conductor or conductor upon doping, this unique structure is conceptually interesting as an "as-assembled" nanocapacitor. Using a well-defined molecular nanoparticle dyad as the model system, the work has more implications in understanding the physical principles underlying the self-assembly of shape amphiphiles constructed using nanobuilding blocks of even larger size, such as gold nanoparticles.

Acknowledgements

This work was supported by NSF (DMR-0906898) and the Collaborative Center in Polymer Photonics of Air Force Research Office. W.-B.Z. gratefully acknowledges the Lubrizol Corporation for a fellowship.

Notes and references

1 J. M. Lehn, *Supramolecular Chemistry: Concepts and Perspectives*, VCH, Weinheim, New York, 1995.
2 J. W. Steed, D. R. Turner and K. J. Wallace, *Core Concepts in Supramolecular Chemistry and Nanochemistry*, John Wiley, Chichester, England, Hoboken, NJ, 2007.
3 G. M. Whitesides, J. P. Mathias and C. T. Seto, *Science*, 1991, **254**, 1312–1319.
4 National Research Council (US), *Committee on Synthetic Hierarchical Structures. Hierarchical Structures in Biology as a Guide for New Materials Technology*, National Academy Press, Washington, DC, 1994.
5 A. Keller and S. Z. D. Cheng, *Polymer*, 1998, **39**, 4461–4487.
6 S. Z. D. Cheng, *Phase Transitions in Polymers: the Role of Metastable States*, Elsevier, Amsterdam, Boston, 2008.
7 R. W. Date and D. W. Bruce, *J. Am. Chem. Soc.*, 2003, **125**, 9012–9013.
8 S. C. Glotzer, M. A. Horsch, C. R. Iacovella, Z. L. Zhang, E. R. Chan and X. Zhang, *Curr. Opin. Colloid Interface Sci.*, 2005, **10**, 287–295.
9 S. C. Glotzer and M. J. Solomon, *Nat. Mater.*, 2007, **6**, 557–562.
10 S. C. Glotzer and J. A. Anderson, *Nat. Mater.*, 2010, **9**, 885–887.
11 R. H. Baney, M. Itoh, A. Sakakibara and T. Suzuki, *Chem. Rev.*, 1995, **95**, 1409–1430.
12 H. W. Kroto, J. R. Heath, S. C. Obrien, R. F. Curl and R. E. Smalley, *Nature*, 1985, **318**, 162–163.
13 D. B. Cordes, P. D. Lickiss and F. Rataboul, *Chem. Rev.*, 2010, **110**, 2081–2173.
14 *Applications of Polyhedral Oligomeric Silsesquioxanes*, ed. C. Hartmann-Thompson, Springer, Dordrecht, 2011.
15 A. Hirsch and M. Brettreich, *Fullerenes: Chemistry and Reactions*, Wiley-VCH, Weinheim, Great Britain, 2005.
16 K. M. Kadish and R. S. Ruoff, *Fullerenes: Chemistry, Physics, and Technology*, Wiley-Interscience, New York, 2000.
17 W. B. Zhang, Y. Tu, R. Ranjan, R. M. Van Horn, S. Leng, J. Wang, M. J. Polce, C. Wesdemiotis, R. P. Quirk, G. R. Newkome and S. Z. D. Cheng, *Macromolecules*, 2008, **41**, 515–517.
18 X. K. Ren, B. Sun, C. C. Tsai, Y. F. Tu, S. W. Leng, K. X. Li, Z. Kang, R. M. Van Horn, X. P. Li, M. F. Zhu, C. Wesdemiotis, W. B. Zhang and S. Z. D. Cheng, *J. Phys. Chem. B*, 2010, **114**, 4802–4810.
19 X. Yu, S. Zhong, X. Li, Y. Tu, S. Yang, R. M. Van Horn, C. Ni, D. J. Pochan, R. P. Quirk, C. Wesdemiotis, W.-B. Zhang and S. Z. D. Cheng, *J. Am. Chem. Soc.*, 2010, **132**, 16741–16744.
20 K. Pielichowski, J. Njuguna, B. Janowski and J. Pielichowski, *Adv. Polym. Sci.*, 2006, **201**, 225–296.
21 D. J. Clarke, J. G. Matisons, G. R. Simon, M. Samoc and A. Samoc, *Appl. Organomet. Chem.*, 2008, **22**, 460–465.
22 D. J. Clarke, J. G. Matisons, G. P. Simon, M. Samoc and A. Samoc, *Appl. Organomet. Chem.*, 2010, **24**, 184–188.
23 Y. H. Wang, J. R. Cao, D. I. Schuster and S. R. Wilson, *Tetrahedron Lett.*, 1995, **36**, 6843–6846.
24 T. Tada, Y. Ishida and K. Saigo, *J. Org. Chem.*, 2006, **71**, 1633–1639.
25 *International Tables for Crystallography*, ed. T. Hahn, D. Reidel Boston, Boston, 1992.
26 W. Clegg, *Crystal Structure Determination*, Oxford University Press, Oxford, New York, 1998.
27 A. R. Bassindale, Z. H. Liu, I. A. MacKinnon, P. G. Taylor, Y. X. Yang, M. E. Light, P. N. Horton and M. B. Hursthouse, *Dalton Trans.*, 2003, 2945–2949.
28 A. J. Waddon and E. B. Coughlin, *Chem. Mater.*, 2003, **15**, 4555–4561.
29 W. I. F. David, R. M. Ibberson, J. C. Matthewman, K. Prassides, T. J. S. Dennis, J. P. Hare, H. W. Kroto, R. Taylor and D. R. M. Walton, *Nature*, 1991, **353**, 147–149.
30 P. A. Heiney, J. E. Fischer, A. R. Mcghie, W. J. Romanow, A. M. Denenstein, J. P. Mccauley, A. B. Smith and D. E. Cox, *Phys. Rev. Lett.*, 1991, **66**, 2911–2914.
31 B. Neises and W. Steglich, *Angew. Chem., Int. Ed. Engl.*, 1978, **17**, 522–524.
32 Z. Z. Bu, Y. Yoon, R. M. Ho, W. S. Zhou, I. Jangchud, R. K. Eby, S. Z. D. Cheng, E. T. Hsieh, T. W. Johnson, R. G. Geerts, S. J. Palackal, G. R. Hawley and M. B. Welch, *Macromolecules*, 1996, **29**, 6575–6581.
33 S. Z. D. Cheng and C. Y. Li, *Textures of Materials*, 2002, **408**, 25–37.
34 S. Q. Zhou, C. Burger, B. Chu, M. Sawamura, N. Nagahama, M. Toganoh, U. E. Hackler, H. Isobe and E. Nakamura, *Science*, 2001, **291**, 1944–1947.
35 H. Murakami, T. Nakanishi, M. Morita, N. Taniguchi and N. Nakashima, *Chem.–Asian J.*, 2006, **1**, 860–867.
36 Y. W. Zhong, Y. Matsuo and E. Nakamura, *J. Am. Chem. Soc.*, 2007, **129**, 3052–3053.
37 J. B. Wang, Y. F. Shen, S. Kessel, P. Fernandes, K. Yoshida, S. Yagai, D. C. Kurth, H. Mohwald and T. Nakanishi, *Angew. Chem., Int. Ed.*, 2009, **48**, 2166–2170.
38 D. Guillon, B. Donnio and R. Deschenaux, in *Fullerene Polymers. Synthesis, Properties and Applications*, ed. N. Martín and F. Giacalone, Wiley-VCH Verlag GmbH & Co. KGaA, Weinheim, 2010.